

Faraday Discussions

Accepted Manuscript



This manuscript will be presented and discussed at a forthcoming Faraday Discussion meeting. All delegates can contribute to the discussion which will be included in the final volume.

Register now to attend! Full details of all upcoming meetings: <http://rsc.li/fd-upcoming-meetings>



This is an *Accepted Manuscript*, which has been through the Royal Society of Chemistry peer review process and has been accepted for publication.

Accepted Manuscripts are published online shortly after acceptance, before technical editing, formatting and proof reading. Using this free service, authors can make their results available to the community, in citable form, before we publish the edited article. We will replace this *Accepted Manuscript* with the edited and formatted *Advance Article* as soon as it is available.

You can find more information about *Accepted Manuscripts* in the [Information for Authors](#).

Please note that technical editing may introduce minor changes to the text and/or graphics, which may alter content. The journal's standard [Terms & Conditions](#) and the [Ethical guidelines](#) still apply. In no event shall the Royal Society of Chemistry be held responsible for any errors or omissions in this *Accepted Manuscript* or any consequences arising from the use of any information it contains.

Effects of molybdenum on the composition and nanoscale morphology of passivated austenitic stainless steel surfaces

*Vincent Maurice, Hao Peng, Lorena H. Klein, Antoine Seyeux,
Sandrine Zanna, Philippe Marcus*

PSL Research University, Chimie ParisTech - CNRS, Institut de Recherche de Chimie Paris, 75005 Paris, France

Abstract

Surface analysis by time-of-flight secondary ion mass spectrometry, X-Ray photoelectron spectroscopy and scanning tunnelling microscopy has been applied to bring new insight on Mo effects on the composition and nanostructure of the passive films grown in sulphuric acid on well-controlled Fe-17Cr-14.5Ni-2.3Mo(100) austenitic stainless steel single crystal surfaces. A duplex hydroxylated oxide matrix, 1.8-1.9 nm thick, is formed with a strong partition between Cr(III) and Fe(III) in the inner and outer layers, respectively. Cr(III) is increasingly enriched by preferential iron oxide dissolution upon passivation and ageing. Ni, only present as oxide traces in the film, is enriched in the alloy underneath. Mo, mostly present as Mo(IV) in the Cr-rich inner layer prior to anodic polarisation, becomes increasingly enriched (up to 16 % of cations) mostly as Mo(VI) in the Fe-rich outer layer of the passive film, with ageing promoting this effect. Metallic Mo is not significantly enriched below the passive film produced from the native oxide covered surface. Mo does not markedly impact the nanogranular morphology of the native oxide film nor its local thickness variations assigned to substrate site effects on Cr(III) enrichment. Site specific preferential passivation still takes place at the (native) oxide-covered step edges of the alloy surface, and transient dissolution remains preferentially located on the terraces. Nanostructures, possibly Mo-containing, and healing local depressions formed by transient dissolution during passivation, appear as a specific effect of the Mo presence. Another Mo effect, observed even after 20 h of passivation, is to prevent crystallisation at least in the Fe-rich outer part of the passive film where it is concentrated mostly as Mo(VI) (*i.e.* molybdate) species.

Keywords: Stainless Steel; Corrosion; Passive films; Molybdenum; XPS; ToF-SIMS; STM

1. Introduction

Stainless steels (SS) owe their high technical importance as structure materials to the formation of a continuous and protective surface oxide layer, the passive film, only a few nanometres thick at ambient temperature and that provides high corrosion resistance in chemically aggressive aqueous environment. Surface analysis, mostly using X-Ray photoelectron spectroscopy (XPS), has demonstrated strong chromium enrichment for passive films on ferritic Fe-Cr,¹⁻¹⁷ and Fe-Cr-Mo^{6,18-20} alloys and on austenitic Fe-Cr-Ni²¹⁻²⁶ and Fe-Cr-Ni-Mo^{21,27-44} alloys. In acidic media, the strong chromium enrichment in the passive range is a consequence of the extremely small dissolution rate of Cr(III) oxide compared to Fe(II)/Fe(III) oxides. It is reduced by the dissolution of chromium as Cr(VI) in the transpassive range, or in alkaline solutions, by the decreasing solubility of Fe(II)/Fe(III) oxides. For Fe-Cr-Ni alloys, no or very little oxidized nickel enters the composition of the passive film and the alloy region underneath the film is enriched in metallic nickel.²¹⁻²⁶ The film thickness is in the range 1-3 nm depending on alloy and passivation conditions.^{6,8,9,11,13,23,25,31,38}

Alloying a few percents of molybdenum improves markedly the resistance to localized corrosion by pitting and Mo bearing stainless steels, including austenitic AISI 316L, offer a better corrosion protection engineering solution in chloride-containing environments where passive film breakdown can be followed by pit initiation. Molybdenum enters the composition of the Cr-enriched passive film as Mo(IV) or Mo(VI) according to various studies, remains at few atomic percent level and has no marked effect on the film thickness.^{21,23,29,31,34,36,38,43} The beneficial role of molybdenum on the corrosion resistance has long been discussed and several effects have been proposed. They can be sorted in two main classes depending on whether Mo is proposed to mitigate passive film breakdown,^{20,21,27,29,32-37,40,44} or to promote

passive film repair.^{19,21,28-30} However, which effect prevails remains a subject of debate or several effects may combine to improve passivity and pitting corrosion resistance.

The atomic structure of passive films on stainless steel has been clarified mostly using scanning tunnelling microscopy (STM) and shown to depend on the Cr content of the alloy and on polarization conditions. For short polarization times in acid solution (≤ 2 hours), long range structural ordering (*i.e.* crystallinity) decreases with increasing Cr content of the alloy.⁴⁵⁻⁴⁸ However, ageing under anodic polarization promotes crystallisation^{13,25} in parallel to the growth of the inner barrier oxide layer, increasingly enriched in Cr(III) as a result of the dehydroxylation of the Cr(III) hydroxide layer preferentially formed in the early stages of passivation.^{3,11,13,25} The observed atomic lattice is consistent with a (111) orientation of the oxygen sublattice (*fcc*) of the main oxide constituent (Cr_2O_3) of the barrier oxide layer.^{13,25,45,46}

The nanostructure of passive films on stainless steel is much less documented despite the fact that intergranular sites joining crystalline grains of the passive film have been shown to play a key role in passivity breakdown and the initiation of localized corrosion.⁴⁹⁻⁵⁴ It is only very recently that STM has been applied to study the morphological modifications brought at the nanometre scale by passivation in acid solution of a Fe-18Cr-13Ni stainless steel surface.⁵⁵ The data could be rationalised in terms of local dissolution of iron-rich oxide species and growth of insoluble Cr(III)-enriched species competing during the passivation process. To our knowledge, no data have been reported on the nanostructure nor the atomic structure of passive films grown on Mo bearing austenitic Fe-Cr-Ni alloys.

In the present work, time-of-flight secondary ion mass spectrometry (ToF-SIMS), XPS and STM have been combined to study the composition and the nanostructure of the passive film formed in sulphuric acid on a Fe-Cr-Ni-Mo alloy of composition close to that of AISI 316L with the objective to get new insight on Mo effects. Well-oriented single crystal

surfaces were used since a well-controlled topography is a prerequisite to resolve the nanoscale morphology of a passivated surface. A complementary *in situ* STM study will be reported separately. To our knowledge, the present work is the first of the kind combining ToF-SIMS, XPS and STM analysis on Mo bearing passivated austenitic stainless steel single crystal surfaces.

2. Experimental

A Fe-17Cr-14.5Ni-2.3Mo (wt%) single crystal oriented parallel to (100) within $\pm 1^\circ$ by Laue back-diffraction was used. The *ex situ* surface preparation was the same as that previously adopted for a Fe-18Cr-13Ni(100) single crystal.^{25,55} It included mechanical polishing, electrochemical polishing and high-temperature annealing in hydrogen reducing atmosphere as previously described. For transfer to the electrochemical cell, the sample was exposed to air (~5 min) leading to the growth of an air-formed native oxide film also characterized by ToF-SIMS, XPS and STM.

The electrochemical cell used for passivation was that of the STM set up. Details on the cell and its cleaning can be found elsewhere.⁵⁶⁻⁶⁰ All potential values given hereafter are with respect to the standard hydrogen electrode (V/SHE). The electrolyte was 0.05 M H₂SO₄(aq) prepared from ultra pure chemicals (Merck, Suprapur[®]) and Millipore[®] water (resistivity > 18 M Ω ·cm). It was not deaerated. Since cathodic reduction of the Cr(III)-containing oxide films irreversibly destroys the terrace topography of the substrate required for high resolution STM as shown previously on chromium,^{61,62} it was avoided. Thus the present work addresses the modifications induced by transformation of the air-formed native oxide into a passive film. The surface was passivated by a potential step from the $E_{\text{OCP}} = -0.17$ V to $E_{\text{pass}} = 0.5$ V, beyond the active peak measured at -0.21 V and in the passive domain ranging up to 0.90 V. The passivation time (t_{pass}) was of 2 or 20 hours. After passivation, the

samples were rinsed with Millipore[®] water, dried with filtered compressed air and transferred for ToF-SIMS, XPS or STM for analysis.

ToF-SIMS analysis was performed using a ToF-SIMS 5 spectrometer (Ion ToF - Munster, Germany) operating at about 10^{-9} mbar. A pulsed 25 keV Bi⁺ primary ion source delivering 1.3 pA current over a $100 \times 100 \mu\text{m}^2$ area was employed for analysis in static SIMS conditions. Depth profiling was carried out by interlacing static analysis with sputtering using a 0.5 keV Cs⁺ sputter beam giving a 12.5 nA target current over a $500 \times 500 \mu\text{m}^2$ area. Analysis was centred inside the eroded crater to avoid edge effects. The profiles were recorded with negative secondary ions which have higher yield for oxide matrices than for metallic matrices. The Ion-Spec software was used for data acquisition and processing.

A VG ESCALAB 250 spectrometer operating at about 10^{-9} mbar was used for XPS analysis. The X-ray source was an Al_{K α} monochromatised radiation ($h\nu=1486.6$ eV). Survey spectra were recorded with a pass energy of 100 eV at a step size of 1 eV and high resolution spectra of the Fe 2p, Cr 2p, Ni 2p, Mo 3d, O 1s, and C 1s core level regions were recorded with a pass energy of 20 eV at a step size of 0.1 eV. Take-off angle of the analysed photoelectrons was 90°. Data processing (curve fitting) was performed using the Avantage software provided by Thermo Electron Corporation. An iterative Shirley-type background and Lorentzian/Gaussian peak shape with a fixed ratio of 30/70 and a tail mix of 100% were used except for the Fe⁰ 2p_{3/2} (91/8 and 11.5%), Cr⁰ 2p_{3/2} (35/65 and 0.66%) and Mo⁰ 3d_{5/2-3/2} (35/65 and 64.7%) metallic components. The binding energies were calibrated by setting the C 1s signal corresponding to olefinic bonds (-CH₂-CH₂-) at 285.0 eV.

The STM setup consisted of a PicoSPM base, a STM S scanner, a PicoScan 2100 controller, and the Picoscan software (Agilent Technologies). W tips electro eroded from 0.25 mm wire in 3M NaOH(aq) were used. All STM images were acquired in air in the constant current topographic mode and were corrected from the background plane. No

filtering was used. Complementary AFM analysis was performed with an Agilent 5500 AFM/SPM microscope operated in intermittent contact (tapping®) mode. In this mode, the cantilever supporting the tip oscillates at its resonant frequency and the feedback loop maintains the oscillation amplitude constant (constant tip-sample interaction) by adjusting the vertical position z of the scanner at each (x,y) data point of the scan. The tip used was made of n-doped silicon and had a nominal radius of curvature less than 10 nm

3. Results and discussion

3.1. Composition studied by ToF-SIMS and XPS

Figure 1 shows the ToF-SIMS negative ion depth profiles for the air-formed native oxide film and the passive films formed at $E_{\text{pass}} = 0.5$ V for 2 and 20 hours on the Mo bearing stainless steel surface. The intensity is plotted in logarithmic scale versus sputtering time for the following selected secondary ions: $^{17}\text{OH}^-$, $^{18}\text{O}^-$, $^{104}\text{Cr}_2^-$, $^{112}\text{Fe}_2^-$ and $^{116}\text{Ni}_2^-$ ($^{16}\text{O}^-$ secondary ions saturate the detector). The $^{18}\text{O}^-$ ion profile is used to define the oxide film region (ending at 84% of the intensity on the plateau⁶³) and the Fe_2^- , Cr_2^- and Ni_2^- ion profiles are used to define the metallic substrate region (starting at the beginning of the intensity plateaus). The intermediate region is assigned to the interfacial region between oxide film and metallic substrate. An intense OH^- signal is measured throughout the region of the oxide films, indicating in all cases a hydroxylated oxide matrix confirmed by XPS.

In Figure 2, the profiles of secondary ions ($^{88}\text{FeO}_2^-$, $^{84}\text{CrO}_2^-$, $^{91}\text{NiO}_2^-$ and $^{128}\text{MoO}_2^-$) characteristic for oxide species present in the films are overlapped using a linear intensity scale. This allows seeing more clearly the evolution after passivation and ageing. The colour-coded dashed lines mark the limits between oxide film and interface regions. Their respective positions do not reflect actual thickness variations of the oxide films as revealed by the thickness values obtained by XPS analysis and discussed further on, possibly owing to

variation of the sputtering yield. It is shown that the FeO_2^- profiles all have their maximum in the outer parts of the oxide film region. Oxidized iron is therefore preferentially located in the outer part of the films regardless of the conditions of formation of the oxide. Its intensity decreases after passivation and ageing, which is linked to the preferential dissolution of the iron oxide generated by passivation in acid solution as expected. The CrO_2^- profiles also exhibit an intensity maximum but located deeper in the films compared to the FeO_2^- profiles. Oxidized chromium is thus preferentially concentrated in the inner part of the films. Its intensity increases significantly after passivation, confirming enrichment of chromium in the passive films.

Throughout the native oxide film, the MoO_2^- profile coincides better with the CrO_2^- profile with a maximum in the inner part of the film. However, after passivation, the MoO_2^- profile peaks in the outer part of the film and coincides with the FeO_2^- profile. It also increases significantly in intensity. This shows that Mo is incorporated in the inner part of the oxide film before passivation and in the outer part, and in larger amounts, after passivation, where oxidized iron is more concentrated.

The NiO_2^- profiles show plateaus of very low intensity throughout the region of the oxide films, showing a homogeneous distribution. The intensity of the NiO_2^- ions, much lower than those of CrO_2^- , FeO_2^- and even MoO_2^- ions, shows that Ni is present only as oxide traces in the films. Passivation and ageing do not seem to generate significant changes of concentration and distribution.

Figure 3 shows the XP Fe 2p, Cr 2p, Ni 2p, Mo 3d and O 1s core level spectra for these samples. Binding energies (BE), full widths at half-maximum (FWHM) and relative intensities of the component peaks obtained by curve fitting are compiled in Table 1. For all samples, nickel is only detected in the metallic state since a single peak component, assigned to $\text{Ni}^0 2p_{3/2}^{42,64}$ of the alloy matrix underneath the films, is observed. The traces of oxidized

nickel observed by ToF-SIMS are then below the detection limit of XPS (< 1 at%). In contrast, several peak components, assigned to different oxidation states, are observed for the other elements constitutive of the alloy: $\text{Fe}^0 2p_{3/2}$,^{6,33,35,42} $\text{Cr}^0 2p_{3/2}$,^{6,31} and the doublet $\text{Mo}^0 3d_{5/2}$ - $\text{Mo}^0 3d_{3/2}$,^{6,31,33,35,38,42} for the metallic matrix of the alloy below the films, and $\text{Fe}^{3+} 2p_{3/2}$,^{6,33,35,42} $\text{Cr}^{3+} 2p_{3/2}$,^{6,31,33,35} and the doublets $\text{Mo}^{4+} 3d_{5/2}$ - $\text{Mo}^{4+} 3d_{3/2}$,^{6,31,33,35,38,42} and $\text{Mo}^{6+} 3d_{5/2}$ - $\text{Mo}^{6+} 3d_{3/2}$,^{6,31,33,35,38,42} for the hydroxylated oxide matrix of the films. Satellite peaks ($\text{Fe}^{\text{sat}} 2p_{3/2}$,^{6,33,35,42} $\text{Cr}^{\text{sat}} 2p_{3/2}$,^{6,31,33,35}) are also observed for the more intense oxidized iron and chromium. The O 1s core level reveals three components, O^{2-} , OH^- and H_2O , assigned to the oxide, hydroxide and water ligands of the films, respectively.^{31,33,42}

The intensity ratio of the hydroxide to oxide components ($I[\text{OH}^-]/I[\text{O}^{2-}]$) markedly increases from 0.36 before passivation to 1.03 and 0.91 after passivation for 2 and 20 h, respectively, showing that the oxide matrix of the passive films is markedly more hydroxylated than that of the native oxide film and with no in-depth significant variations as shown by the ToF-SIMS profiles (Figure 1). For the passivated samples, an additional $\text{Cr}^{3+(\text{hyd})} 2p_{3/2}$ component assigned to Cr(III) ions bonded to an hydroxylated oxide matrix^{33,35,42} was used for curve fitting the Cr 2p spectra. In contrast, adding such a component was not necessary for peak fitting the Fe 2p and Mo 3d spectra. Still, it appears reasonable to consider that the fitted $\text{Fe}^{3+} 2p_{3/2}$, $\text{Mo}^{4+} 3d$ and $\text{Mo}^{6+} 3d$ components also include cations bonded to hydroxide ligands. For all samples, no $\text{Fe}^{2+} 2p_{3/2}$ component at $708.3 \pm 0.2 \text{ eV}$ ⁶⁵⁻⁶⁷ was necessary to fit Fe 2p spectra, showing that iron cations are essentially in the 3+ oxidation state. However, it cannot be excluded that a small fraction of them are in the 2+ oxidation state. The slight decrease of the $I[\text{OH}^-]/I[\text{O}^{2-}]$ ratio for the 20 h passivated sample reflects the process of dehydroxylation generated by ageing in the passive state, in agreement with previous data.^{11,13,25}

The intensity ratio $I[\text{Cr}^{3+(\text{ox})(\text{hyd})}]/I[\text{Fe}^{3+(\text{ox})}]$ increases from 0.55 for the native oxide film to 1.13 (2 h sample) and 1.63 (20 h sample) for the passive films, highlighting the enrichment in oxidized chromium in the films after passivation and ageing in the passive state due to preferential dissolution of the iron oxide in acid medium. This confirms the trend measured by ToF-SIMS and is in agreement with previous data.^{11,13,25} The intensity ratio $I[\text{Mo}^{(\text{ox})}]/I[\text{Mo}^0]$, increasing from 0.65 before passivation to 1.95 and 2.32 after passivation for 2 and 20 h, respectively, is indicative of the Mo enrichment in the oxide film after passivation. Mo enrichment is also obtained by ageing from 2 to 20 hours, but it is much less pronounced. The intensity ratio $I[\text{Mo}^{6+(\text{ox})}]/I[\text{Mo}^{4+(\text{ox})}]$ also increases, from 0.44 before passivation to 2.62 and 2.60 after passivation for 2 and 20 h, respectively. Molybdenum is thus preferentially present in the 4+ oxidation state in the native oxide film and in the 6+ oxidation state after passivation, in agreement with previous work.^{29,31,42} This ratio remains constant during ageing. These results show that the passivation in acid medium has a marked effect on the Mo content in the film and the fractions of cations Mo^{6+} and $\text{Mo}^{4+(\text{ox})}$. Ageing produces a weaker effect.

Based on these ToF-SIMS and XPS data, the duplex model presented in Figure 4 was used to calculate the composition and thickness of the oxide films and the composition of the alloy underneath. For all films, the model assumes an essentially oxide/hydroxide matrix with partition of iron and chromium in the outer and inner layers, respectively. Molybdenum is considered to be homogeneously distributed in the inner layer for the native oxide film and in the outer layer of the passive films. This duplex model differs from those previously proposed for Fe-Cr-Ni-Mo alloys passivated in acid and neutral solutions for which the outer layer consisted of chromium hydroxide and the inner layer of mixed iron/chromium oxide.^{21,34,38,42} It is however consistent with previous Auger electron spectroscopy depth profiling data showing maximum Cr enrichment in the inner part of the film.^{6,18,28} Clearly, our ToF-SIMS

data do not support a hydroxide/oxide partition as no peak is observed in the outer region of the film for the OH^- , CrO_2^- and also CrO^- (not shown) ion profiles. The low OH^- peak at the beginning of the ToF-SIMS profiles and the low intensity H_2O 1s XP component suggest a slight surface hydration. It is neglected in the model because of the low $I[\text{H}_2\text{O}]/I[\text{OH}^-]+I[\text{O}^{2-}]$ XP ratio ($< 10\%$). Also, an abrupt interface between the outer and inner layers of the films appears as a simplification according to the ToF-SIMS data, and decreasing and increasing concentrations of iron and chromium oxides, respectively, could be a more realistic description.

The thickness of each layer of the oxide films and the concentration in Fe, Cr, Ni and Mo of the outer and inner layer of the films and of the modified alloy underneath the films can be calculated from the intensities of the $\text{Fe}^{3+} 2p_{3/2}$, $\text{Cr}^{3+} 2p_{3/2}$ ($I[\text{Cr}^{3+(\text{ox})} 2p_{3/2}] + I[\text{Cr}^{3+(\text{hyd})} 2p_{3/2}]$), $\text{Mo}^{4+} 3d_{3/2}$, $\text{Mo}^{6+} 3d_{3/2}$, $\text{Fe}^0 2p_{3/2}$, $\text{Cr}^0 2p_{3/2}$, $\text{Ni}^0 2p_{3/2}$ and $\text{Mo}^0 3d_{3/2}$ component peaks based on the exponential attenuation of the photoelectron intensity with increasing escape depth from the surface. The procedure uses intensity ratios and is described in details elsewhere.⁶⁸ The results are compiled in Table 2.

The total thickness is found to be 1.8-1.9 nm for the passive films, in agreement with previous data (1.4-1.7 nm) for Mo implanted stainless steel after passivation in sulphuric acid.⁴² The inner layer is thicker than the outer layer. The total film thickness does not vary markedly after passivation, however with slight thickening of the inner layer and thinning of the outer layer. The ageing process has no significant effect on the thickness. Chromium is enriched in all studied films and this enrichment is more pronounced after passivation, due to the preferential dissolution of iron oxide in acid solutions.^{29,38,42,43,69} Cr(III) ions represent 67% and 72% of the metal cations for the passive films formed for 2 and 20 hours, respectively. Nickel oxide, observed by ToF-SIMS, is present only as traces not detected by XPS in this study, in agreement with previous work.^{29,42} As a consequence, the alloy

underneath the passive film is slightly depleted in metallic Cr (~15 at% for the passivated surfaces as compared to ~18 at% in the bulk alloy) and strongly enriched in metallic Ni (~33 at% for the passivated surfaces as compared to ~14 at% in the bulk alloy), also in agreement with previous work.^{29,42} This enrichment in Ni is more pronounced for the passive films than for the native oxide film, consistently with the preferential dissolution of iron upon passivation. Ageing in the passive state has little effect on the Cr enrichment in the passive film and no significant effect on the enrichment in Ni in the modified alloy region below the films.

Concerning molybdenum, although the concentration is high, about 11 and 16 % of metal cations in the outer layer of the passive films after 2 and 20 h, respectively, it is only about 4 % if referred to the whole film. For the native oxide film in which Mo is concentrated in the inner layer, this value is 2.1 %. In the modified alloy layers underneath the films, the Mo concentration (1.3-1.5 at%) is not significantly different from that in the bulk alloy (1.3 at%). We can therefore conclude that passivation causes Mo enrichment, concentrated in the outer part of the film and mostly in the 6+ oxidation state as discussed above, in agreement with previous works concluding to the presence of molybdates.^{29,31,42} Ageing in the passive state causes further enrichment of the outer layer in Mo, most likely due to preferential dissolution of iron oxide in the passive state. However, our data show that the passivation-induced Mo enrichment in the oxide film does not modify significantly the Mo concentration in the metallic layers underneath. This is in contrast with previous studies^{21,31,38} that reported Mo enrichment below the passive film in a polycrystalline alloy (on which more dissolution may have taken place during passivation).

3.2. Nanoscale morphology studied by STM and AFM

Figure 5 shows STM topographic data obtained at the nanometre scale on the Fe-17Cr-14.5Ni-2.3Mo(100) single crystal stainless steel surface covered by the air-formed native

oxide film. The observed topography is characterized by a succession of steps and terraces. Terraces, up to hundreds of nanometres in width, alternate with series of narrower terraces from 30 to 54 nm in width. This terrace topography is that of the substrate. The steps separating the terraces result from the residual disorientation of the surface from the nominal crystallographic orientation (100) obtained only on the terraces. The step height ranges from 0.9 to 1.3 nm. Given the reticular distance of two successive (100) planes of the alloy (0.18 nm from bulk values), the measured steps are multi-atomic (from 5 to 7 (100) planes high).

Both on the wider (Figure 5b) and narrower (Figure 5c) terraces of the alloy, the presence of three main surface levels is clearly evidenced. It is confirmed by AFM images (not shown). The corresponding top (T), medium (M) and bottom (B) topographic levels are marked in red, green and blue, respectively, in Figure 5b and 5c and in the extracted line profile in Figure 5d. Table 3 compiles the height difference (ΔZ) values measured between these three main surface levels by STM. It also includes values obtained by AFM. The very good agreement between the STM and AFM values confirms the topographic origin of the surface levels and allows ruling out any significant artefact in the STM measurement caused by electronic effect. The height difference between the topmost (T) and lowest (B) surface levels ($\Delta Z_{T-B} = 1.02 \pm 0.20$ nm) is significantly lower than the equivalent thickness of the native oxide film measured by XPS (1.7 nm). It appears thus consistent with a native oxide film fully covering the alloy substrate but presenting local deviations (of up to about ± 0.5 nm as inferred from the ΔZ_{T-B} value of about 1 nm) from an average thickness value of 1.7 nm. The formation of three main topographic levels was also observed for on a Fe-18Cr-13Ni(100)⁵⁵ surface prepared in the same conditions, and ΔZ values are listed in Table 3 for comparison.

Figure 5c evidences the nanogranular morphology of the air-formed oxide film. Grains, better resolved by STM than by AFM, are observed on each of the three main surface

levels of the oxide film, *i.e.* independently of the local thickness. Their lateral grain dimension is 5.29 ± 0.86 nm and the apparent depth measured in the boundaries separating the grains is 0.35 ± 0.05 nm as measured by STM (Table 3, the AFM resolution does not allow to extract reliable values of these parameters). The apparent depth measured between the grains is consistent with full coverage of the substrate by the oxide, even in the thinnest (~ 1.2 nm) regions of the films. This nanogranular morphology is assigned to the formation of the film by a nucleation and growth mechanism, with the small dimensions of the grains being a direct consequence of the high density of oxide nuclei formed by exposure at ambient pressure and room temperature. Table 3 shows no significant variation of the dimensions of the grains owing to the presence of Mo in the alloy, showing again that its presence in small amounts does not affect the nanoscopic morphological characteristics of the native oxide film.

Quite interestingly, one also notices in Figure 5c that the step edges are nearly saturated with grains associated with the topmost surface level of the oxide film and that the terraces are covered with grains preferentially associated with the medium and lowest surface levels. This site differentiation is indicative of a relation between the nucleation and growth mechanism of the oxide film and its local thickness. The XPS data in Table 2 show that the native oxide is enriched in Cr(III) as a result of the preferential oxidation of chromium of the prepared alloy surface. It is then likely that the oxide formed at step edges and in the T areas is locally not only thicker, as directly observed by STM, but also more enriched in Cr(III). For balance, the locally thinner oxide formed on the terraces in the M and B areas would be then less enriched in Cr(III). Crystallographic defect sites of the alloy surface, such as step edges, would thus promote nucleation of the oxide film, as a result of a decreased energy barrier for oxidation of both iron and chromium. They would also promote local thickening and Cr(III) enrichment in the oxide as a result of faster growth preferentially consuming chromium by surface diffusion also from the neighbouring areas. As a result, the neighbouring areas would

be less Cr(III)-enriched and thinner. The B areas of the oxide film would correspond to the thinnest and least enriched in Cr(III) since they have provided chromium for the enrichment of both the M and T areas. On the terraces, such promoting effects on local thickening and Cr(III) enrichment would be less pronounced however with other crystallographic features playing a role as suggested by the nearly square arrangements adopted by the T areas (Figure 5b). Comparison with the data for the non Mo bearing alloy shows no significant effect of molybdenum on the formation of the three topographic surface levels (separated by similar ΔZ values if one considers dispersion, Table 3) and their site differentiation. Thus, it appears that the nucleation and growth mechanism and resulting local thickness variation of the native oxide film are not significantly modified by the presence of small amount (3.6 % cation fraction) of Mo in the inner Cr-rich layer of the native oxide film.

No crystalline lattice could be measured on this surface at higher resolution, suggesting the growth of an amorphous air-formed oxide film, like on the Fe-18Cr-13Ni(100) surface.⁵⁵

Figure 6 shows STM topographic data for the Fe-17Cr-14.5Ni-2.3Mo(100) passivated for 2 h. It is evidenced that anodic polarization in the passive range does not destroy the typical terrace topography of the substrate produced by the surface preparation, and modifications must be appreciated more locally. Three main surface levels are still present (as marked in Figure 6a and shown by the line profile in Figure 6c), however with significant increases of the ΔZ values separating them (Table 3) also measured by AFM. Two phenomena compete during passivation in acid solution: (i) transient dissolution, predominantly of soluble Fe(II) species, either pre-existing on the surface oxide film or produced by anodic oxidation and consuming the alloy, which contributes to lower the apparent surface level, and (ii) growth, predominantly of insoluble Cr(III) and Mo(VI) species produced by anodic oxidation, which contributes to raise the apparent surface level. Both

contribute to increase the ΔZ values between the local surface levels. XPS shows no significant variation of the total thickness of the surface oxide film after passivation and thus, the observed variations must be dominated by passivation-induced transient dissolution. It is expected that transient dissolution will vary depending on the local thickness and composition of the pre-formed native oxide film. In the lowest surface level areas, dissolution of the alloy should be promoted since the film is thinner and dissolution of the oxide should also be promoted since the film is locally less Cr(III) enriched as discussed above. Conversely, in the topmost surface level areas where the film is the thickest and possibly the most Cr(III)-rich, dissolution of both the alloy and the oxide should be less pronounced. This mechanism would account for the observed increase of the difference between the surface topographic levels after passivation. The role of Mo on these passivation-induced local modifications of the stainless steel surface is difficult to assess. Table 3 compiles similar data for Mo-free Fe-18Cr-13Ni(100) surface passivated in similar conditions (3 h at 0.5 V) in 0.5 M H₂SO₄. The ΔZ values also increase after passivation and are similar to those measured for the Mo bearing surface, showing no significant effect of the presence of Mo. Only the ΔZ_{M-B} value varies differently, which remains unexplained at present. Mo is known for decreasing dissolution in the active state. This effect is not confirmed by the ΔZ values that are the same after 2-3 h of passivation. However, the present data do not strictly address the active-passive transition since they are obtained on surfaces initially covered by the air-formed native oxide. Data obtained after shorter polarisation time and/or at lower potential (*e.g.* in the pre-passive region) could be more conclusive on the effect of Mo on the passivation-induced local modifications of the stainless steel surface associated with the competing mechanisms of transient dissolution and oxide growth.

The image in Figure 6c also reveals the nanogranular morphology of the passive film. The lateral dimensions of the grains are larger than for the native oxide film (Table 3). This

increase suggests that oxide growth generated by passivation occurs both perpendicularly to the surface so as to compensate the effect of transient dissolution (no thickness increase of the film is measured by XPS) and laterally. The lateral growth is probably due to a phenomenon of coalescence accompanying the transformation of native oxide to passive film. Comparison with data obtained on the Mo-free Fe-18Cr-13Ni(100) surface passivated in similar conditions, that also show an increase of the grain lateral dimension,⁵⁵ points to no significant effect of molybdenum given the dispersion of the measurements.

One also notices in Figure 6a,b that the step edges are still saturated with grains associated with the topmost surface level of the passive film and that, on the narrower terraces, depressions corresponding to the lowest surface level are located in the centre of the terraces. This confirms site differentiation after passivation-induced modifications. The absence of depressions at the step edges suggests that local transient dissolution, accompanying the formation of the passive film as discussed above, was attenuated, or even blocked, at these sites. This is consistent with the native oxide-covered alloy surface being more enriched in chromium along the step edges and less in the terraces in the vicinity of step edges as discussed above. A similar site differentiation was observed for the passivated Mo-free Fe-18Cr-13Ni(100) surface,⁵⁵ and it appears not affected by the presence of Mo.

Figure 6 also reveals an interesting feature of the passivated surface. The depressions (some are marked by circles in Figure 6a,b) observed on the narrower terraces appear partially filled by nanostructures. In some cases, the depressions even appear fully filled and only their contours remain identified. The presence of such nanostructures suggests late growth of the passive film in the sites where transient dissolution was stronger or redeposition of dissolved corrosion products. The formation of these structures tends to homogenize the topography of the passivated surface, healing nanostructural heterogeneities (*i.e.* local depressions) created by transient dissolution. Such nanostructures were not observed on the passivated Mo-free Fe-

18Cr-13Ni(100) surface,⁵⁵ and it is suggested that their formation is promoted by the presence of Mo.

Figure 7 shows STM topographic data for the Fe-17Cr-14.5Ni-2.3Mo(100) passivated for 20 h. All nanoscopic features of the passivated surface are confirmed: subsisting terrace topography of the substrate (Figure 7a); three main topographic levels on the terraces (Figure 7b), site-specific formation of depressions (Figure 7a) and nanogranular morphology of the passive film (Figure 7c). The values of the height differences between topographic surface levels and grain dimensions compiled in Table 3 show no significant variation caused by ageing in the passive state from 2 to 20 hours. Also, comparison with data for passivated Mo-free Fe-18Cr-13Ni(100) surface⁵⁵ shows no marked effect of the presence of Mo on these nanoscopic features. The presence of nanostructures (marked by circles in Figure 7a) filling the depressions created by passivation-induced transient dissolution is confirmed for the Mo bearing alloy surface.

No crystalline lattice could be measured on these passivated surfaces at higher resolution, either after 2 or 20 h of passivation. Figure 6d and Figure 7c show two examples of higher resolution images that display no sign of crystallisation of the oxide films, even after ageing for 20 h. Typically, when a crystalline oxide film forms, images obtained at this magnification display the terrace topography associated with the termination of the oxide lattice.^{13,25,48,55-58,62} This is not observed in the presented images and could not be obtained in the present study, in contrast with data obtained for Mo-free austenitic stainless steel surfaces studied in similar conditions of passivation and measurement.^{13,25,55} This suggests that the passive films produced in these conditions on the Mo bearing stainless steel surface retain an amorphous structure, at least in their outer parts, in the conditions tested in this work, including after 20 h ageing under anodic polarisation. It is possible that Mo, concentrated in the outer parts of the passive films, stabilizes the formation of an amorphous outer layer of

molybdate-containing Fe-rich oxide. This amorphous outer layer could prevent the observation by STM of the inner Cr-rich oxide layer, possibly crystallized as usually observed after ageing on Mo-free stainless steel surfaces.^{13,25,55}

4. Conclusion

The oxide films grown in air or by anodic polarisation in sulphuric acid (0.05 M H₂SO₄(aq); 0.5 V/SHE; 2 and 20 h) on (100)-oriented Fe-17Cr-14.5Ni-2.3Mo single crystal stainless steel surfaces can be described by a duplex hydroxylated oxide matrix with a strongly Cr(III)-enriched inner layer and a strongly Fe(III)-enriched outer layer. The oxide matrix becomes markedly hydroxylated after passivation ($[\text{OH}^-]/[\text{O}^{2-}] \sim 1$). The total thickness (1.8-1.9 nm) does not markedly increase after passivation, however with a slight increase of the inner part compensated by a decrease of the outer part. Chromium is increasingly enriched, up to 67 and 72 % of metal cations, by preferential iron oxide dissolution upon passivation and aging, and depleted in the alloy below the film. Nickel, present in the films as oxide traces below the detection limit of XPS (< 1 at%), is enriched in the alloy underneath. Molybdenum, mostly present as Mo(IV) in the inner part of the air-formed film, becomes concentrated and increasingly (up to 16 % of metal cations) enriched mostly as Mo(VI) in the outer part of the passive film with ageing promoting enrichment. No significant Mo enrichment is observed in the alloy below the passive film produced by anodic polarization of the native oxide covered surface.

The air-formed native oxide film has a nanogranular morphology and develops 3 main topographic surface levels reflecting local variations (± 0.5 nm) of the thickness (1.7 nm in average), assigned to local variations of the Cr(III) enrichment promoted by substrate site effects. Passivation increases the lateral dimensions of the nanograins, like for a Mo-free stainless steel surface. It also increases the height difference between surface levels, also owing to the local effect of thickness and Cr(III) enrichment on the transient dissolution

occurring during passivation but with no marked effect of Mo. Site specific preferential passivation takes place at the oxide-covered step edges of the alloy surface, most likely more Cr(III)-enriched, with transient dissolution preferentially located on the less Cr(III)-enriched terraces, like observed in the absence of Mo. Local nanostructures, possibly Mo-containing, growing in the depression formed by local transient dissolution and healing them, appear as a specific effect observed in the presence of molybdenum. Another Mo effect, observed even after 20 h of passivation, is to prevent crystallisation at least in the outer part of the passive film where it is concentrated mostly as Mo(VI) (*i.e.* molybdate) species.

References

1. M. Seo, N. Sato, *Surf. Sci.*, 1979, **86**, 601.
2. I. Olefjord, B. Brox, in: *Passivity of Metals and Semiconductors*, ed. M. Froment, Elsevier, Amsterdam, 1983, pp. 561.
3. G. Hultquist, M. Seo, T. Leitner, C. Leygraf, N. Sato, *Corrosion Sci.*, 1987, **27**, 937.
4. D. F. Mitchell, M. Graham, *Surf. Interf. Anal.*, 1987, **10**, 259.
5. S. Mischler, H. J. Mathieu, D. Landolt, *Surf. Interf. Anal.*, 1988, **11**, 182.
6. P. Marcus, I. Olefjord, *Corrosion Sci.*, 1988, **28**, 589.
7. C. Calinski, H.-H. Strehblow, *J. Electrochem. Soc.*, 1989, **136**, 1328.
8. R. Kirchheim, B. Heine, H. Fischmeister, S. Hofmann, H. Knotte, U. Stolz, *Corrosion Sci.*, 1989, **29**, 899.
9. J. E. Castle, J. H. Qiu, *Corrosion Sci.*, 1989, **29**, 591.
10. C. Hubschmid, H. J. Mathieu, D. Landolt, *Proceedings of the 12th International Corrosion Congress*, NACE, Houston, 1993, pp. 3913.
11. W. P. Yang, D. Costa, P. Marcus, *J. Electrochem. Soc.*, 1994, **141**, 2669.
12. S. Haupt, H.-H. Strehblow, *Corrosion Sci.*, 1995, **37**, 43.
13. V. Maurice, W. Yang, P. Marcus, *J. Electrochem. Soc.*, 1996, **143**, 1182.
14. L.J. Oblonsky, M.P. Ryan, H.S. Isaacs, *J. Electrochem. Soc.*, 1998, **145**, 1922.
15. D. Hamm, K. Ogle, C.-O.A. Olsson, S. Weber, D. Landolt, *Corrosion Sci.*, 2002, **44**, 1443.

16. P. Keller, H.-H. Strehblow, *Corrosion Sci.*, 2004, **46**, 1939.
17. C.-O.A. Olsson, D. Landolt, *Electrochim. Acta*, 2003, **48**, 1093.
18. S. Mischler, A. Vogel, H. J. Mathieu, D. Landolt, *Corrosion Sci.*, 1991, **32**, 925-944.
19. K. Hashimoto, K. Asami, K. Teramoto, *Corrosion Sci.*, 1979, **19**, 3-14
20. M.-W. Tan, E. Akiyama, A. Kawashima, K. Asami, K. Hashimoto, *Corrosion Sci.*, 1995, **37**, 1289-1301.
21. I. Olefjord, B.-O. Elfström, *Corrosion Sci.*, 1982, **38**, 46.
22. B. Brox, I. Olefjord, *Surf. Interf. Anal.*, 1988, **13**, 3.
23. E. De Vito, P. Marcus, *Surf. Interf. Anal.*, 1992, **19**, 403.
24. C.-O.A. Olsson, S.E. Hörnström, *Corrosion Sci.*, 1994, **36**, 141.
25. V. Maurice, W. Yang, P. Marcus, *J. Electrochem. Soc.*, 1998, **145**, 909.
26. T. Yamamoto, K. Fushimi, M. Seo, S. Tsuru, T. Adachi, H. Habazaki, *Corrosion Sci.*, 2009, **51**, 1545.
27. K. Sugimoto, Y. Sawada, *Corrosion Sci.*, 1977, **17**, 425-445.
28. H. Ogawa, H. Omata, I. Itoh, H. Okada, *Corrosion*, 1978, **34**, 52-60.
29. I. Olefjord, *Materials Science and Engineering*, 1980, **42**, 161-171.
30. W. Yang, R.-C. Ni, H.-Z. Hua and A. Pourbaix, *Corrosion Sci.*, 1984, **24**, 691-707.
31. I. Olefjord, B. Brox, U. Jelvestam, *J. Electrochem. Soc.*, 1985, **132**, 2854-2861.
32. A. R. Brooks, C. R. Clayton, K. Doss, Y. C. Lu, *J. Electrochem. Soc.*, 1986, **133**, 2459-2464.
33. C. R. Clayton, Y. C. Lu, *J. Electrochem. Soc.*, 1986, **133**, 2465-2473.
34. Y. C. Lu, C. R. Clayton, A. R. Brooks, *Corrosion Sci.*, 1989, **29**, 863-880.
35. C. R. Clayton, Y. C. Lu, *Corrosion Sci.*, 1989, **29**, 881-898.
36. J. E. Castle J. H. Qiu, *Corrosion Sci.*, 1989, **29**, 591-603.
37. J. E. Castle J. H. Qiu, *Corrosion Sci.*, 1989, **29**, 605-616.
38. I. Olefjord, L. Wegrelius, *Corrosion Sci.*, 1990, **31**, 89-98.
39. H. Habazaki, A. Kawashima, K. Asami, K. Hashimoto, *Corrosion Sci.*, 1992, **33**, 225-236.
40. D. D. Macdonald, *J. Electrochem. Soc.*, 1992, **139**, 3434-3449.
41. A. Elbiache and P. Marcus, *Corrosion Sci.*, 1992, **33**, 261-269.
42. E. De Vito and P. Marcus, *Surf. Interf. Anal.*, 1992, **19**, 403-408.

-
43. N. E. Hakiki, M. D. C. Belo, A. M. P. Simões, M. G. S. Ferreira, *J. Electrochem. Soc.*, 1998, **145**, 3821-3829.
44. M. Bojinov, G. Fabricius, T. Laitinen, K. Mäkelä, T. Saario, G. Sundholm, *Electrochim. Acta*, 2001, **46**, 1339-1358.
45. M. P. Ryan, R. C. Newman, G. E. Thompson, *Philosophical Mag. B*, 1994, **70**, 241.
46. M. P. Ryan, R. C. Newman, G. E. Thompson, *J. Electrochem. Soc.*, 1994, **141**, L164.
47. C. L. McBee, J. Kruger, *Electrochim. Acta*, 1972, **17**, 1337.
48. H. Nanjo, R. C. Newman, N. Sanada, *Appl. Surf. Sci.*, 1997, **121**, 253.
49. V. Maurice, L. H. Klein, P. Marcus, *Electrochem. Solid State Lett.*, 2001, **4**, B1.
50. V. Maurice, T. Nakamura, L. Klein, P. Marcus, in *Local Probe Techniques for Corrosion Research*, eds. R. Oltra, V. Maurice, R. Akid, P. Marcus, EFC Publications N° 45, Woodhead Publishing Ltd, Cambridge, 2007, pp. 71.
51. P. Marcus, H.-H. Strehblow, V Maurice, *Corrosion Sci.*, 2008, **50**, 2698.
52. A. Seyeux, V. Maurice, P. Marcus, *Electrochem. Solid State Lett.*, 2009, **12**, C25.
53. T. Massoud, V. Maurice, F. Wiame, L. H. Klein, A. Seyeux, P. Marcus, *J. Electrochem. Soc.*, 2012, **159**, C351.
54. T. Massoud, V. Maurice, F. Wiame, L. H. Klein, A. Seyeux, P. Marcus, *Corrosion Sci.*, 2013, **69**, 245.
55. T. Massoud, V. Maurice, L. H. Klein, P. Marcus, *J. Electrochem. Soc.*, 2013, **160**, C232-C238.
56. D. Zuili, V. Maurice, P. Marcus, *J. Electrochem. Soc.*, 2000, **147**, 1393.
57. A. Seyeux, V. Maurice, L. H. Klein, P. Marcus, *J. Solid State Electrochem.*, 2005, **9**, 337.
58. A. Seyeux, V. Maurice, L. H. Klein, P. Marcus, *J. Electrochem. Soc.*, 2006, **153**, B453.
59. V. Maurice, L. H. Klein, H.-H. Strehblow, P. Marcus, *J. Phys. Chem. C*, 2007, **111**, 16351.
60. N. Li, V. Maurice, L. H. Klein, P. Marcus, *J. Phys. Chem. C*, 2012, **116**, 7062.
61. V. Maurice, W.-P. Yang, P. Marcus, *J. Electrochem. Soc.*, 1994, **141**, 3016-3027.
62. D. Zuili, V. Maurice, P. Marcus, *J. Phys. Chem. B*, 1999, **103**, 7896.
63. ASTM E 1438-91 (1996), Standard Guide for Measuring Widths of Interfaces in Sputter Depth Profiling Using SIMS.
64. P. Marcus, J. M. Grimal, *Corrosion Sci.*, 1992, **33**, 805-814.
65. N. S. McIntyre, D. G. Zetaruk, *Anal. Chem.*, 1977, **49**, 1521-1529.

-
66. V. Stambouli, C. Palacio, H. J. Mathieu, D. Landolt, *Appl. Surf. Sci.*, 1993, **70-71**, 240-244.
67. G. Bhargava, I. Gouzman, C. M. Chun, T. A. Ramanarayanan, S. L. Bernasek, *Appl. Surf. Sci.*, 2007, **253**, 4322-4329.
68. H. Peng, PhD Thesis, Thèse de Doctorat, Université Pierre et Marie Curie, 2014.
69. J. B. Lumsden, R. W. Staehle, *Scripta Metallurgica*, 1972, **6**, 1205-1208.

Table 1

Table 1 Binding energy (BE), full-width at half-maximum (FWHM) and relative intensity (RI) of the XP core level components obtained by peak fitting for the native and passive oxide films formed on the Fe-17Cr-14.5Ni-2.3Mo(100) single crystal stainless steel surface. The relative intensity is normalised to the most intense component of the core level.

	Native oxide film			Passive film (2 h)			Passive film (20 h)		
	BE (eV)	FWHM (eV)	RI	BE (eV)	FWHM (eV)	RI	BE (eV)	FWHM (eV)	RI
Fe ⁰ 2p _{3/2}	706.7	0.8	1.00	706.7	0.8	1.00	706.7	0.8	1.00
Fe ^{3+(ox)} 2p _{3/2}	709.8	3.5	0.67	710.0	3.5	0.69	709.8	3.4	0.38
Fe ^{sat} 2p _{3/2}	712.3	3.5	0.20	712.5	3.5	0.21	711.8	3.4	0.22
Cr ⁰ 2p _{3/2}	573.7	1.3	0.46	573.7	1.3	0.55	573.7	1.3	0.56
Cr ^{3+(ox)} 2p _{3/2}	576.2	2.4	1.00	575.9	1.7	0.92	575.9	1.7	0.90
Cr ^{3+(hyd)} 2p _{3/2}	--	--	--	577.0	1.7	1.00	577.0	1.7	1.00
Cr ^{sat} 2p _{3/2}	577.8	2.4	0.23	578.3	1.7	0.37	578.4	1.7	0.30
Mo ⁰ 3d _{5/2}	227.2	0.8	1.00	227.3	0.7	0.71	227.3	0.7	0.60
Mo ⁰ 3d _{3/2}	230.4	0.8	0.67	230.4	1.0	0.47	230.4	0.7	0.40
Mo ^{4+(ox)} 3d _{5/2}	228.5	2.5	0.45	228.9	2.3	0.38	229.0	2.5	0.39
Mo ^{4+(ox)} 3d _{3/2}	231.6	2.5	0.30	232.2	2.3	0.26	232.2	2.5	0.26
Mo ^{6+(ox)} 3d _{5/2}	231.6	2.5	0.20	231.8	2.5	1.00	232.0	2.5	1.00
Mo ^{6+(ox)} 3d _{3/2}	234.7	2.5	0.13	235.0	2.5	0.67	234.8	2.5	0.67
Ni ⁰ 2p _{3/2}	852.8	1.0	1.00	852.7	1.1	1.00	852.7	1.1	1.00
O ²⁻ 1s	530.0	1.4	1.00	530.1	1.5	0.98	530.1	1.5	1.00
OH ⁻ 1s	531.5	1.4	0.36	531.7	1.5	1.00	531.6	1.5	0.91
H ₂ O 1s	532.7	1.4	0.09	533.0	1.5	0.21	533.1	1.5	0.22
C-C 1s	285.0	1.3	1.00	284.8	1.5	1.00	284.7	1.5	1.00

Table 2

Table 2 Thickness and chemical composition of the duplex native and passive oxide films on the Fe-17Cr-14.5Ni-2.3Mo(100) single crystal stainless steel surface as obtained from XPS analysis.

		<i>Global film</i>	<i>Outer layer</i>	<i>Inner layer</i>	<i>Modified alloy</i>
Native oxide film	d (nm)	1.7	0.7	1.0	----
	[Fe] (at%)	41.2	100	----	60.8
	[Cr] (at%)	56.7	----	96.4	13.1
	[Ni] (at%)	----	----	----	24.6
	[Mo] (at%)	2.1	----	3.6	1.5
Passive film (2h)	d (nm)	1.9	0.6	1.3	----
	[Fe] (at%)	29.2	89.1	----	51.0
	[Cr] (at%)	67.2	----	100	14.7
	[Ni] (at%)	----	----	----	32.8
	[Mo] (at%)	3.6	10.9	----	1.5
Passive film (20h)	d (nm)	1.8	0.5	1.3	----
	[Fe] (at%)	23.3	83.9	----	50.5
	[Cr] (at%)	72.2	----	100	15.1
	[Ni] (at%)	----	----	----	33.1
	[Mo] (at%)	4.5	16.1	----	1.3

Table 3

Table 3 Height differences between bottom (B), medium (M) and top (T) topographic surface levels (ΔZ_{M-T} , ΔZ_{B-M} and ΔZ_{B-T}), grain lateral dimension (L_G) and intergranular depth (ΔZ_{IG}) for the native oxide film and passive films grown on the Fe-17Cr-14.5Ni-2.3Mo(100) single crystal stainless steel surface, and comparison with data for the Fe-18Cr-13Ni(100) surface.

<i>Sample</i>	<i>Technique</i>	ΔZ_{T-M} (nm)	ΔZ_{M-B} (nm)	ΔZ_{T-B} (nm)	L_G (nm)	ΔZ_{IG} (nm)	<i>Ref.</i>
Native oxide on FeCrNiMo	STM	0.49 ± 0.06	0.55 ± 0.12	1.02 ± 0.20	5.29 ± 0.86	0.35 ± 0.05	This work
	AFM	0.61 ± 0.07	0.60 ± 0.08	1.49 ± 0.15	---	---	This work
Passive film on FeCrNiMo ($E_{\text{pass}} = 0.50$ V ; $t_{\text{pass}} = 2$ h)	STM	0.97 ± 0.20	1.22 ± 0.17	2.27 ± 0.25	11.49 ± 2.56	0.54 ± 0.15	This work
	AFM	0.92 ± 0.10	0.96 ± 0.13	2.00 ± 0.30	---	---	This work
Passive film on FeCrNiMo ($E_{\text{pass}} = 0.50$ V ; $t_{\text{pass}} = 20$ h)	STM	1.17 ± 0.16	1.30 ± 0.21	2.14 ± 0.22	8.73 ± 2.86	0.51 ± 0.18	This work
	AFM	0.90 ± 0.13	0.97 ± 0.17	2.06 ± 0.26	---	---	This work
Native oxide on FeCrNi	STM	0.36 ± 0.05	0.72 ± 0.09	1.21 ± 0.09	5.43 ± 0.71	0.25 ± 0.06	55
Passive film on FeCrNi ($E_{\text{pass}} = 0.50$ V ; $t_{\text{pass}} = 3$ h)	STM	1.09 ± 0.23	0.64 ± 0.15	1.97 ± 0.20	9.57 ± 1.73	0.60 ± 0.23	55
Passive film on FeCrNi ($E_{\text{pass}} = 0.50$ V ; $t_{\text{pass}} = 20$ h)	STM	1.03 ± 0.20	1.06 ± 0.19	1.95 ± 0.26	8.24 ± 2.00	0.49 ± 0.17	This work

Figure captions

Figure 1 ToF-SIMS negative ion depth profiles of the air-formed native oxide film (a) and passive films formed on the Fe-17Cr-14.5Ni-2.3Mo(100) single crystal stainless steel surface in 0.05 M H₂SO₄(aq) at 0.5 V/SHE for 2 hours (b) and 20 hours (c). Dashed lines mark the limits between oxide film, interface and substrate regions.

Figure 2 Comparison of the ToF-SIMS depth profiles of ⁸⁸FeO₂⁻, ⁸⁴CrO₂⁻, ⁹¹NiO₂⁻ and ¹²⁸MoO₂⁻ ions for the air-formed native oxide film (Nat.) and passive films formed on Fe-17Cr-14.5Ni-2.3Mo(100) single crystal stainless steel surface in 0.05 M H₂SO₄(aq) at 0.5 V/SHE for 2 hours (Pass. 2h) and 20 hours (Pass 20h). The colour-coded dashed lines mark the limits between oxide film and interface regions.

Figure 3 XP core level Fe 2p, Cr 2p, Ni 2p, Mo 3d and O 1s spectra for the air-formed native oxide film and passive films formed on Fe-17Cr-14.5Ni-2.3Mo(100) single crystal stainless steel surface in 0.05 M H₂SO₄(aq) at 0.5 V/SHE for 2 and 20 hours.

Figure 4 Duplex model for calculating the chemical composition of the oxide films formed on the Fe-17Cr-14.5Ni-2.3Mo(100) single crystal stainless steel surface

Figure 5 STM topographic data for the Fe-17Cr-14.5Ni-2.3Mo(100) stainless steel surface covered by the air-formed native oxide film (a) top view image: Z range $\Delta Z = 8$ nm, bias voltage $V_t = -1.6$ V, tunnel current $I = 0.5$ nA. (b) top view image: $\Delta Z = 2$ nm, $V_t = -1.7$ V, $I = 0.5$ nA. (c) top view image: $\Delta Z = 2$ nm, $V_t = -1.6$ V, $I = 0.5$ nA. (d) Height profile along the segment in (b). The three main topographic levels are marked B (bottom), M (medium) and T (top) symbols.

Figure 6 STM topographic data for the Fe-17Cr-14.5Ni-2.3Mo(100) stainless steel surface passivated in 0.05 M $H_2SO_4(aq)$ at 0.5 V/SHE for 2 hours (a) top view image: Z range $\Delta Z = 5$ nm, bias voltage $V_t = -1.7$ V, tunnel current $I = 0.5$ nA. (b) top view image: $\Delta Z = 5$ nm, $V_t = -1.7$ V, $I = 0.5$ nA. (c) Height profile along the segment in (a). (d) top view image: $\Delta Z = 4$ nm, $V_t = -1.7$ V, $I = 0.5$ nA. The three main topographic levels are marked B (bottom), M (medium) and T (top) symbols. Circles point depressions partially filled by nanostructures.

Figure 7 STM topographic data for the Fe-17Cr-14.5Ni-2.3Mo(100) stainless steel surface passivated in 0.05 M $H_2SO_4(aq)$ at 0.5 V/SHE for 20 hours (a) top view image: Z range $\Delta Z = 4$ nm, bias voltage $V_t = -1.9$ V, tunnel current $I = 0.5$ nA. (b) Height profile along the segment in (a). (c) top view image: $\Delta Z = 4$ nm, $V_t = -3.0$ V, $I = 0.5$ nA. The three main topographic levels are marked B (bottom), M (medium) and T (top) symbols. Circles point depressions partially filled by nanostructures.

Figure 1

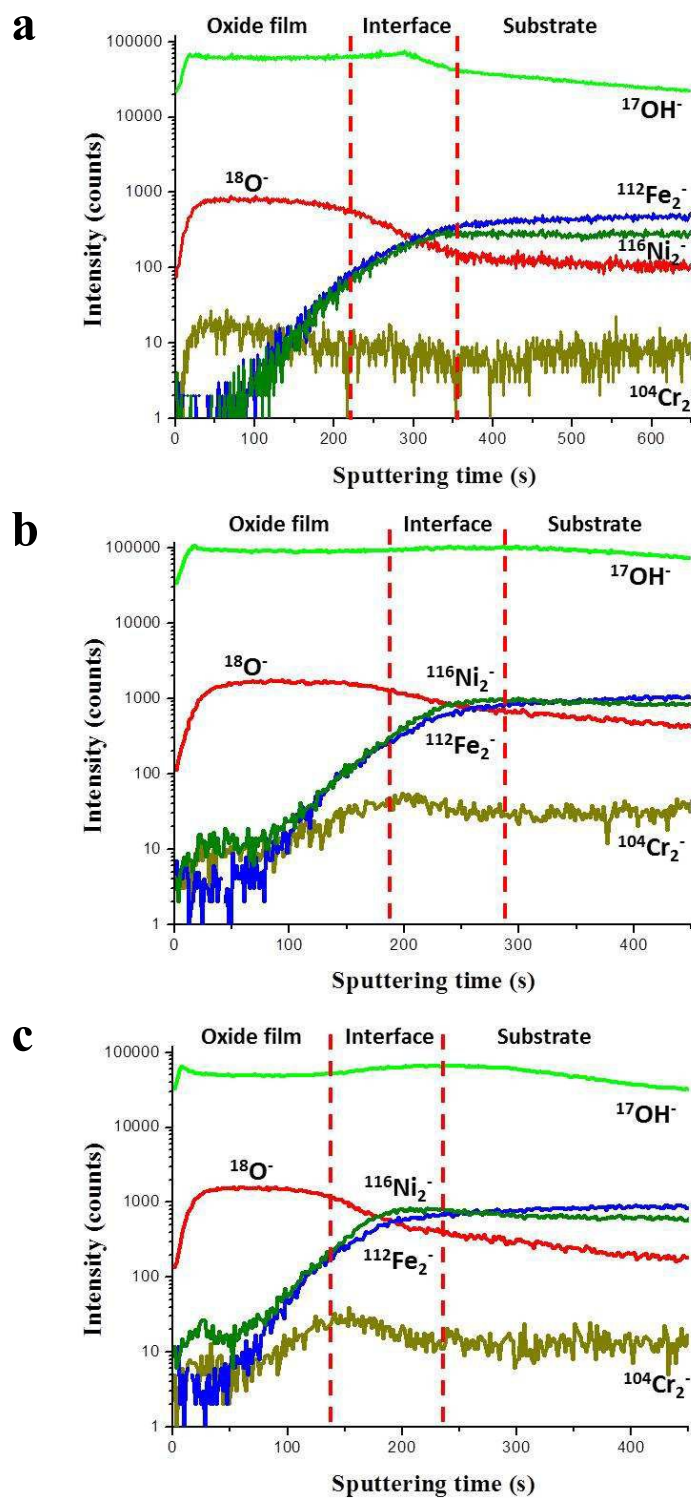


Figure 2

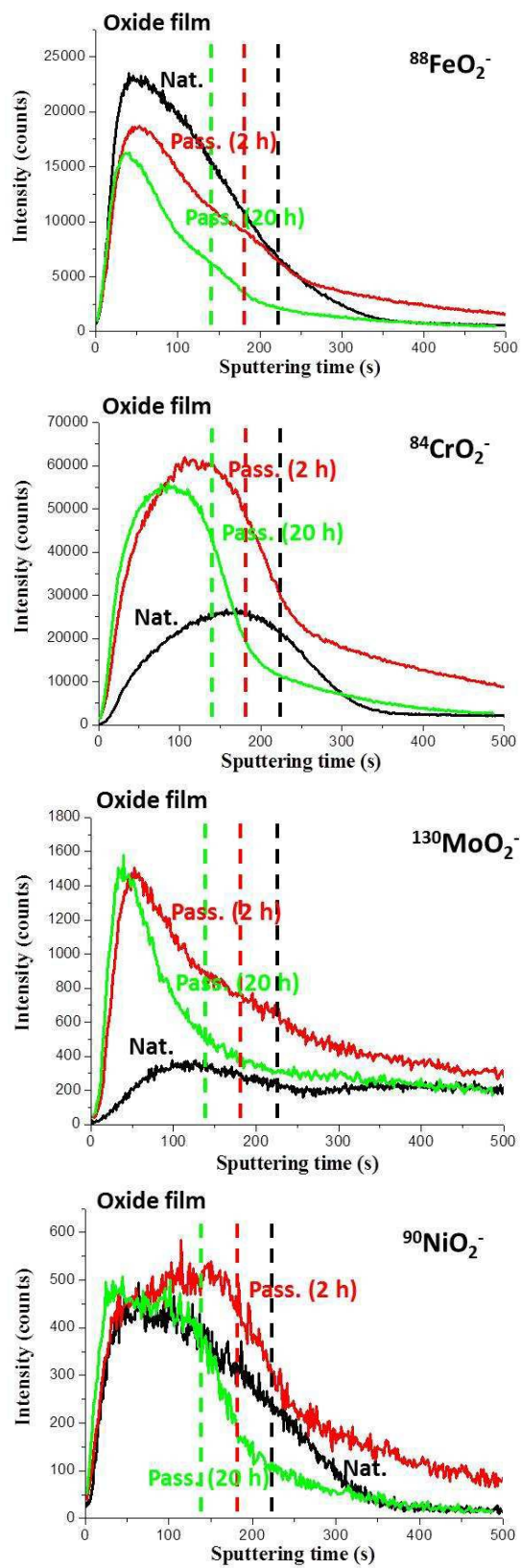


Figure 3

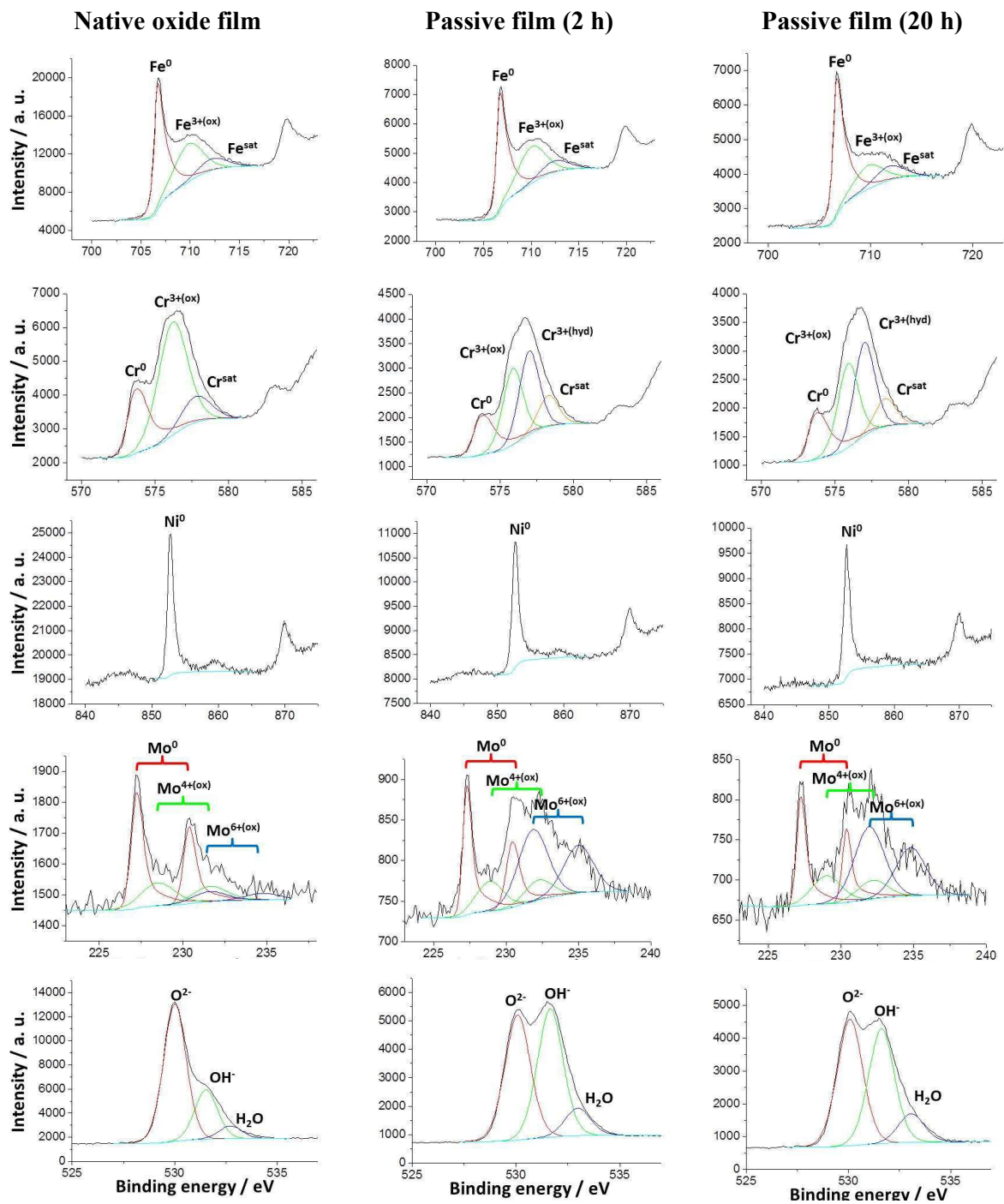


Figure 4

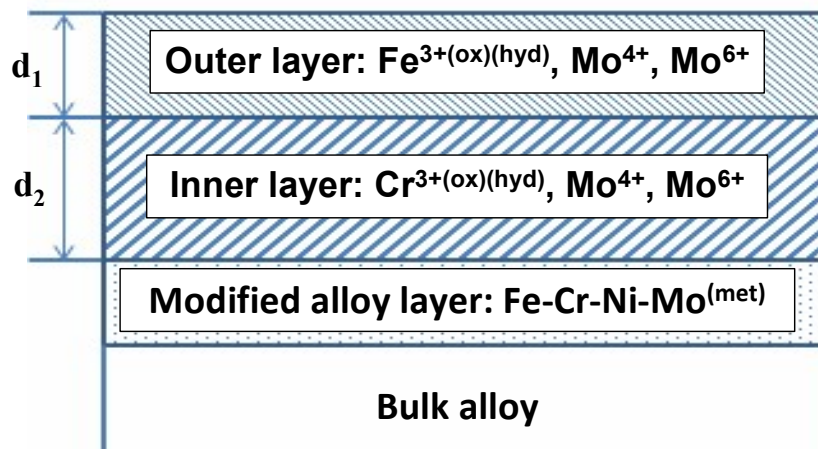


Figure 5

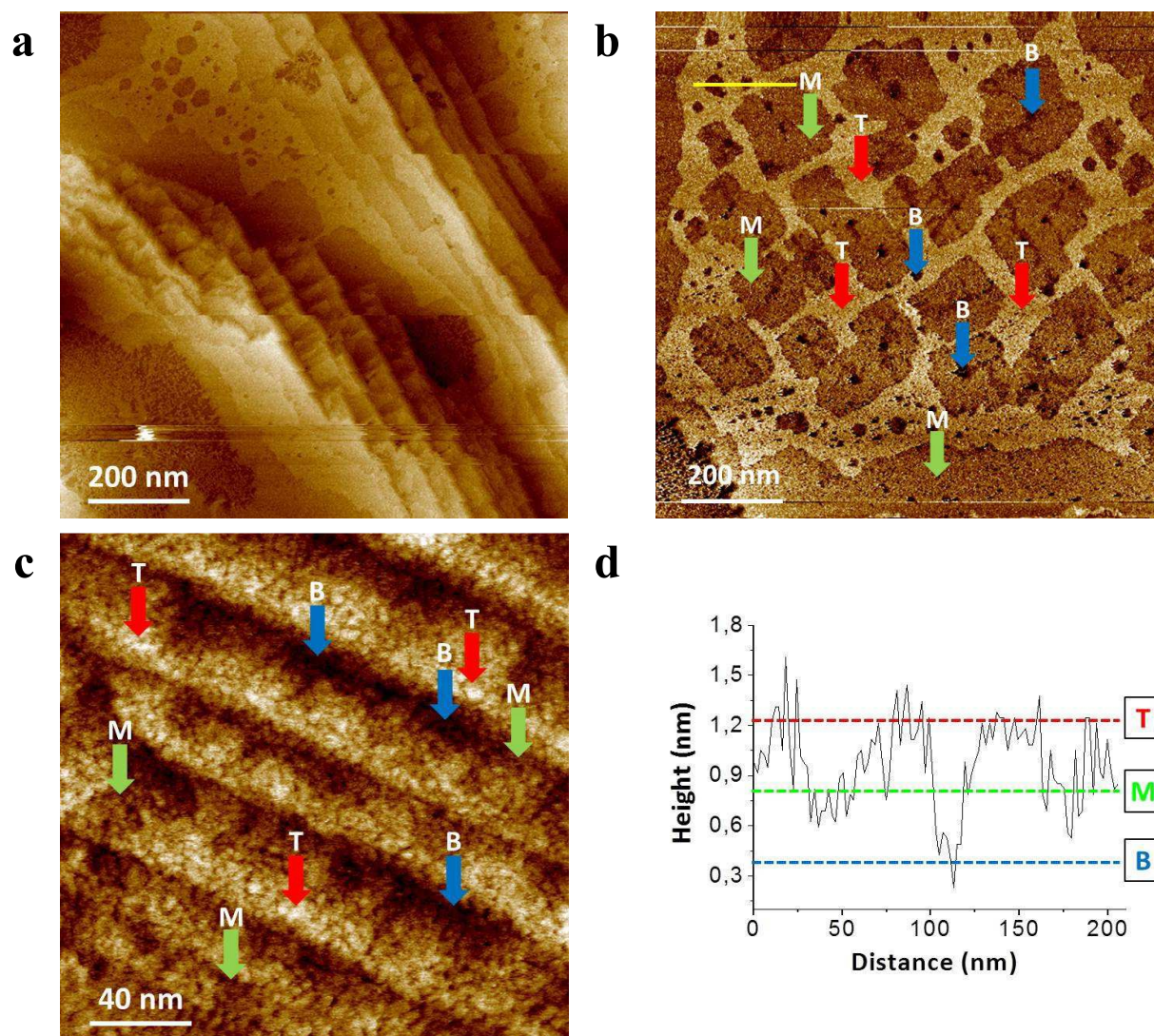


Figure 6

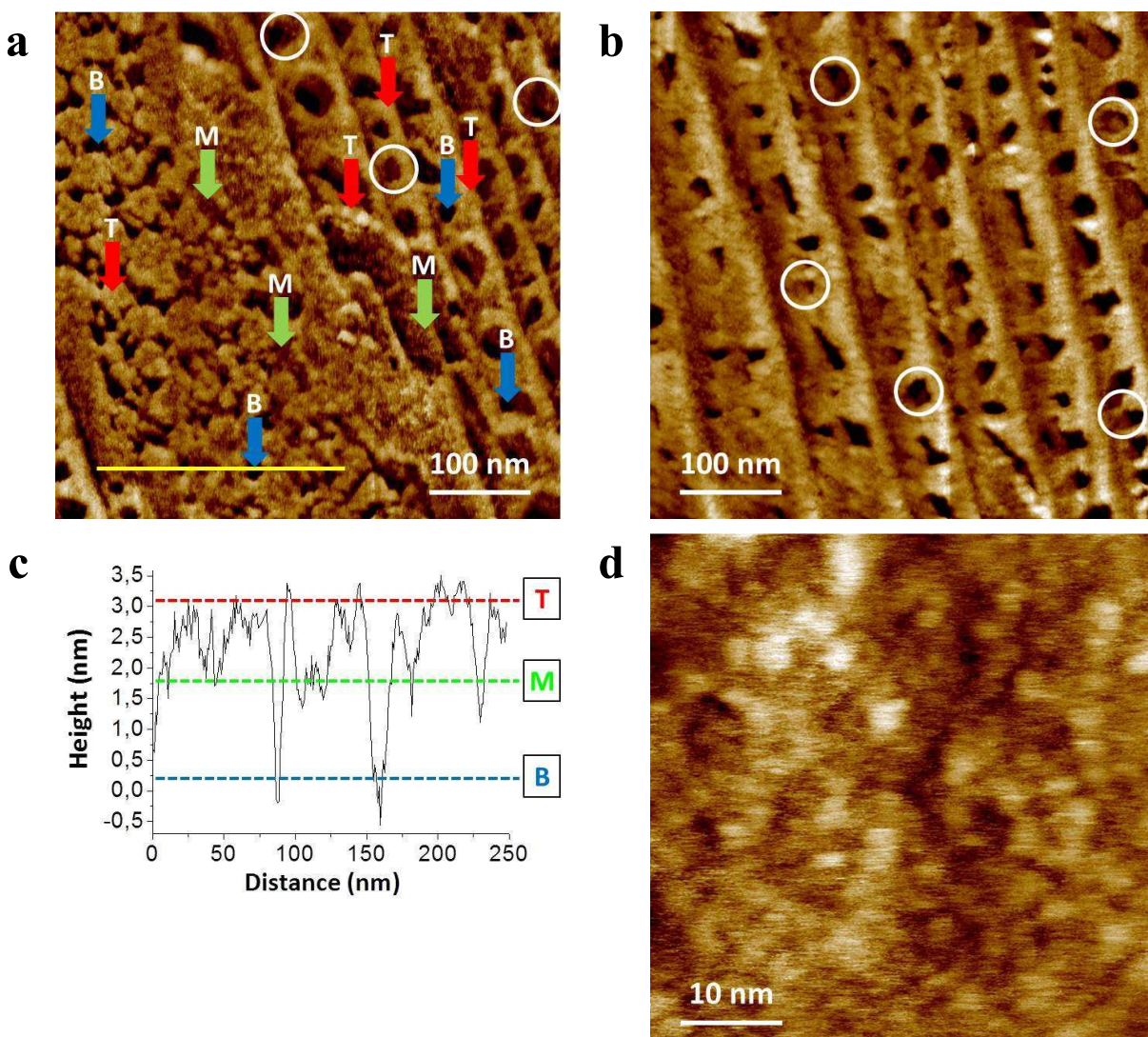


Figure 7

